

Improving the mean-field approximation in continuous models of population dynamics with nonlocal dispersal: applications to vegetation pattern formation

Anudeep Surendran^{1,†}, David Pinto-Ramos^{1,†}, Rafael Menezes^{1,2,†}, and Ricardo Martinez-Garcia^{1,3,*}

¹Center for Advanced Systems Understanding (CASUS); Helmholtz-Zentrum Dresden-Rossendorf (HZDR), Görlitz, Germany

²Ecology Department, University of São Paulo, São Paulo, SP, Brazil

³ICTP South American Institute for Fundamental Research & Instituto de Física Teórica, Universidade Estadual Paulista - UNESP, São Paulo SP, Brazil

[†]These authors contributed equally to this work and share first authorship

*Corresponding author: r.martinez-garcia@hzdr.de

Abstract

Spot patterns, in which vegetation patches form a hexagonal lattice, are frequent in nature and could serve as an early-warning indicator of abrupt vegetation collapses. Consequently, they have been intensively studied using both individual-based models and density-based field equations. Yet, the relationship between these two approaches remains unclear, particularly in scenarios where vegetation dynamics exhibit strong long-range spatial correlations and traditional mean-field approximations fail. To solve this issue, we develop a new method that refines mean-field approximations by describing both the dynamics of the biomass density field and its spatial correlations. This new approach harnesses the strengths of both individual and density-based models, treating spatial correlations explicitly and allowing for the identification of spatial instabilities resulting in periodic patterns. Our results indicate that this new approximation predicts the parameter regimes where regular periodic patterns emerge more accurately than mean-field models, suggesting that it could provide a more robust framework to perform further nonlinear analysis.

1 Introduction

Populations of sessile organisms exhibit diverse spatial patterns, from randomly scattered individuals to aggregates that are periodically distributed in space [1, 2]. The latter are particularly interesting from a modeling point of view because they raise questions about how interactions operating at the scale of organisms lead to organized structures at much larger spatial scales [3–5]. Moreover, regular patterns could enhance population productivity, resilience, and resistance to higher environmental stresses, underscoring their ecological significance [6–9].

Plants in water-limited ecosystems provide a good system to investigate regular pattern formation in populations of sessile and semi-sessile organisms [10]. Several studies using aerial and satellite images from different locations have identified a variety of patterns in these systems, including gaps, stripes, rings, labyrinths, and spots [11–14]. These patterns are primarily shaped by environmental factors such as gradients in resource availability, interactions between plants and other organisms, and local topography [14–19]. For example, along a gradient of increasing aridity, pattern shapes shift from gaps to labyrinths and ultimately to spots [12]. Therefore, these spot patterns, where approximately circular patches of vegetation form a hexagonal lattice in a matrix of bare soil [20], could indicate proximity to non-vegetated states [8].

This potential role as an early-warning indicator of desertification processes makes spot patterns ecologically relevant. However, the long timescales governing vegetation dynamics and the limited availability of long-term datasets pose challenges for empirically investigating the ecological significance of vegetation patterns [but see 21, 22]. Alternatively, researchers have used spatially explicit theoretical models to explain both how spot patterns could form and the types of desertification processes they might precede [23–27]. Broadly, existing models can be classified into two categories: discrete individual-based (IBM), and continuous density-based models.

IBMs describe a population as a spatial distribution of point-like organisms that reproduce and die according to probabilistic rules that encode different interactions and dispersal mechanisms [28, 29]. These models are built at the level of individual plants, which makes it possible to study spatial patterns resolving the patch structure, and are easy to simulate computationally. However, the computational overhead associated with these simulations scales rapidly with the system size and the complexity of interactions, and analytical techniques to study them are limited to providing predictions of population size and its spatial correlations at equilibrium [30–32].

In continuous models, on the other hand, the vegetation biomass is a field that changes in space and time following a differential equation [33, 34]. This approach is easier to treat mathematically, which makes it possible to predict the dynamics of certain spatial processes, such as the direction of ‘desertification’ fronts [35]. However, density-based models do not resolve individual plants, which

limits how much they inform about patch composition. This limitation turns them inappropriate for studying random and irregular aggregated patterns [36] unless they consider environmental heterogeneity [37–40] or demographic fluctuations explicitly [41–44].

Continuous models based on differential equations and IBMs are, thus, two complementary ways of investigating vegetation patterns and their ecological consequences, each presenting its limitations and strengths. Moreover, even though there are techniques to derive effective continuous models starting from individual-based dynamical rules [45], very few studies follow this approach, which makes it unclear how IBMs and continuous models based on field equations relate and compare. Here, we tackle this issue by analyzing a simple IBM with a minimal set of ingredients leading to regular spatial patterns. The existence of regular patterns makes this model tractable both using analytical approximations to the individual-based stochastic dynamics and a continuous equation for the biomass density field. Combining these two approaches, we show how a mean-field density equation fails in predicting the pattern formation regime, contrary to previous studies with motile organisms [46, 47], and use spatial moment dynamics equations to introduce a novel method that corrects this discrepancy. This corrected density equation could be useful for performing further nonlinear analyses that exploit the strengths of density-based models [48], such as determining transitions between pattern states, the existence of localized structure solutions, or the dynamics of fronts, to mention a few.

2 Model formulation and analytical approximations

2.1 Description of the stochastic dynamics

At the individual level, we model the population dynamics using a spatially explicit stochastic logistic model [28, 36]. We assume that organisms are identical except for their location and consider that they inhabit a two-dimensional landscape Ω , with area $|\Omega| = A$. Therefore, the state of the population at a given time t is fully determined by the set of plant locations \mathbf{x}_i [$i = 1, \dots, N(t)$], where $N(t)$ is the number of plants at time t . Altogether, these locations define a spatial pattern $p(\mathbf{x}, t) = \sum_i \delta(\mathbf{x} - \mathbf{x}_i)$.

To keep our analysis as simple as possible, we consider a simple birth-death dynamics in continuous time [36]. The i -th individual, located at \mathbf{x}_i , reproduces and disperses a new organism at location \mathbf{x} at a rate

$$B_i(\mathbf{x}) = b \phi_D(\mathbf{x} - \mathbf{x}_i), \quad (2.1)$$

where $\phi_D(\mathbf{x} - \mathbf{x}_i)$ is a dispersal kernel that defines the probability that individuals born at location \mathbf{x}_i establish at location \mathbf{x} . Because it acts as a probability density function, ϕ_D must be normalized to

unity. Several empirical studies have measured these dispersal kernels across species and investigated their importance in shaping ecological dynamics [49, 50]. Here, we follow a more common choice in the modeling literature and assume this kernel to be a Normal distribution centered at \mathbf{x}_i and with variance s [28, 32]. Conversely, each organism in a given spatial distribution p dies at a rate

$$D_i(p) = d + g \sum_{j \neq i} \phi_C(\mathbf{x}_i - \mathbf{x}_j), \quad (2.2)$$

where the first term on the right side corresponds to baseline mortality, and the second term accounts for density-dependent effects due to intraspecific competition. ϕ_C is the competition kernel that weighs the influence of an organism at \mathbf{x}_j on the focal individual at \mathbf{x}_i [51]. The competition kernel models the negative impact of neighbors on the fitness of a focal individual due to, for example, intraspecific competition for shared limited resources. The shape of the competition kernel is a key ingredient in determining the type of spatial patterns that can form [46, 52]. In the simulations, we used two different types of competition kernels. The first type is a Gaussian kernel with mean zero and standard deviation, r_c . The second is a top-hat competition kernel, defined by the form:

$$\phi_C(\mathbf{x}_i - \mathbf{x}_j) = \begin{cases} \frac{1}{\pi r_c^2} & \text{if } |\mathbf{x}_i - \mathbf{x}_j| \leq r_c, \\ 0 & \text{otherwise.} \end{cases} \quad (2.3)$$

In both cases, r_c defines the characteristic spatial scale of the competition.

Note that, while we present a conceptual model and use dimensionless parameters, every model parameter quantifies a process driving plant population dynamics in natural scenarios and can thus be linked to different plant traits. The variance of the dispersal kernel s is a proxy for the distance over which a plant disperses its seeds. The characteristic spatial range of competition, r_c , defines the distance over which plants' roots compete for belowground shared resources such as water and minerals. Finally, the intrinsic birth and death rates, b and d , represent the rates at which an individual plant reproduces and dies, respectively, while in isolation. Therefore, even though our model does not model a specific plant species, approximated parameter values can be extracted from empirical measurements of dispersal kernels, root systems, or plant life-history studies [53, 54].

The combined effect of birth and death terms in Eq.(2.1) and Eq.(2.2) produces a simple logistic-like birth-death dynamics. We performed all IBM simulations in a square domain of lateral length $L = 20$, using periodic boundary conditions. We fixed this domain size to ensure that it is sufficiently large compared to the interaction scales s and r_c to observe meaningful patterns within the domain. A summary of key parameters of the model is provided in Table 1.

Symbol	Parameter	Value
b	Intrinsic birth rate	3.05
d	Intrinsic death rate	0.305
s	Dispersal range	0 – 1.25
r_c	Spatial range of competition	0 – 4
g	Strength of competition	1

Table 1: Model parameters and typical values.

2.2 Spatial moment dynamics equations

The discrete dynamics in Section 2.1 can be approximated at the macroscale in terms of the moments of the population spatial pattern. For the kind of spatial point process considered in the IBM, the first spatial moment, $Z_1(t)$, represents the average plant density within the population [31]. More formally, the first spatial moment for a given vegetation spatial pattern, $p(\mathbf{x}, t)$, over a two-dimensional landscape Ω , with area $|\Omega| = A$ is defined as,

$$Z_1(t) = \frac{1}{A} \int_{\Omega} p(\mathbf{x}, t) d\mathbf{x}. \quad (2.4)$$

The second spatial moment, $Z_2(\boldsymbol{\xi}, t)$, is the average density of pairs of plants separated by a displacement $\boldsymbol{\xi}$ [55], which is formally defined as,

$$Z_2(\boldsymbol{\xi}, t) = \frac{1}{A} \int_{\Omega} p(\mathbf{x}, t) (p(\mathbf{x} + \boldsymbol{\xi}, t) - \delta(\boldsymbol{\xi})) d\mathbf{x}. \quad (2.5)$$

Similarly, the third spatial moment, $Z_3(\boldsymbol{\xi}, \boldsymbol{\xi}', t)$, corresponds to the average density of triplet of plants separated by displacements $\boldsymbol{\xi}$ and $\boldsymbol{\xi}'$, respectively [56]. Again, for a given vegetation spatial pattern $p(\mathbf{x}, t)$, the third spatial moment is defined as,

$$Z_3(\boldsymbol{\xi}, \boldsymbol{\xi}', t) = \frac{1}{A} \int_{\Omega} p(\mathbf{x}, t) (p(\mathbf{x} + \boldsymbol{\xi}, t) - \delta(\boldsymbol{\xi})) \times \quad (2.6)$$

$$(p(\mathbf{x} + \boldsymbol{\xi}', t) - \delta(\boldsymbol{\xi}') - \delta(\boldsymbol{\xi}' - \boldsymbol{\xi})) d\mathbf{x},$$

where the delta functions in Eq. (2.5) and Eq. (2.6) prevent counting pairs and triplets with repeated plants. Finally, we can obtain the radial correlation function from the definition of the second spatial moment (2.5) as

$$C(r, t) = \frac{1}{2\pi r Z_1^2(t)} \int Z_2(r, \theta, t) r d\theta. \quad (2.7)$$

Note that normalizing the correlation function in Eq. (2.7) by $Z_1^2(t)$ —the density of pairs of plants under complete spatial randomness (alternatively termed uniform patterns)—ensures that

$C(r, t) = 1$ in the absence of spatial patterns (Fig. 1A, circle panel) [51]. As such, when $C(r, t) > 1$, the measured spatial structure has more pairs separated by a distance r than a population with complete spatial randomness. We refer to these types of spatial patterns as clustered spatial patterns (Fig. 1A: Triangle panel). On the other hand, when $C(r, t) < 1$, there are fewer plant pairs with a separation distance r than if they were in a spatially random configuration. We refer to these patterns as over-dispersed or segregated spatial patterns (Fig. 1A: Diamond panel).

To derive the dynamical equations for the spatial moments, we first need to compute the continuum analogue of the discrete neighbor-dependent death rate in Eq. (2.2). According to the definition in Eq. (2.2), the contribution of a neighboring individual located at a displacement $\boldsymbol{\xi}$, to the death rate of a focal plant is given by the competition kernel, $\phi_C(\boldsymbol{\xi})$. Now, the probability of an individual having a neighbor at a displacement, $\boldsymbol{\xi}$, is given by $Z_2(\boldsymbol{\xi}, t)/Z_1(t)$ (see [56, 57] for detailed derivations). Consequently, the expected per-capita death rate can be obtained by multiplying $Z_2(\boldsymbol{\xi}, t)/Z_1(t)$ by $g\phi_C(\boldsymbol{\xi})$ and integrating over all possible displacements as,

$$D_1(t) = d + \frac{g}{Z_1(t)} \int \phi_C(\boldsymbol{\xi}) Z_2(\boldsymbol{\xi}, t) d\boldsymbol{\xi}. \quad (2.8)$$

Since birth events are assumed to be neighbor-independent in the IBM [Eq. (2.1)], the expected per-capita birth rate is simply $B_1(t) = b$.

The dynamics of the first spatial moment are entirely governed by the balance between birth and death events because these two are the only processes influencing population size in our model. Therefore, the time evolution of the first spatial moment is:

$$\frac{d}{dt} Z_1(t) = (b - D_1(t)) Z_1(t). \quad (2.9)$$

Note that the dynamics of the first moment, in turn, are governed by the second moment through the death rate term in Eq. (2.8).

Next, we derive the dynamics of the second spatial moment. To this end, we first compute the death rate, $D_2(\boldsymbol{\xi}, t)$, for a plant that is paired with another at a displacement $\boldsymbol{\xi}$. Remember that the neighbor-dependent component of the death rate for a single plant, $D_1(t)$, was conditioned on the presence of another plant at a displacement $\boldsymbol{\xi}$. In a similar fashion, the neighbor-dependent component of $D_2(\boldsymbol{\xi}, t)$, is conditioned on the presence of a third plant at a displacement $\boldsymbol{\xi}'$. This conditional probability of having another plant located at a displacement $\boldsymbol{\xi}'$ is $Z_3(\boldsymbol{\xi}, \boldsymbol{\xi}', t)/Z_2(\boldsymbol{\xi}, t)$. Following the same procedure as in Eq. (2.8), the expected death rate of a plant in pair with another at a separation displacement $\boldsymbol{\xi}$ can be computed by multiplying $Z_3(\boldsymbol{\xi}, \boldsymbol{\xi}', t)/Z_2(\boldsymbol{\xi}, t)$ by $g\phi_C(\boldsymbol{\xi})$ and

integrating over all possible displacements as follows:

$$D_2(\boldsymbol{\xi}, t) = d + \frac{g}{Z_2(\boldsymbol{\xi}, t)} \int \phi_C(\boldsymbol{\xi}') Z_3(\boldsymbol{\xi}, \boldsymbol{\xi}', t) d\boldsymbol{\xi}' + g\phi_C(\boldsymbol{\xi}). \quad (2.10)$$

Note that the additional factor of $g\phi_C(\boldsymbol{\xi})$ in the third term of Eq. (2.10) accounts for the direct influence of the individual at displacement $\boldsymbol{\xi}$.

We compute the dynamics of the second spatial moment by examining how the density of pairs at displacement $\boldsymbol{\xi}$ changes, balancing pair loss through death and creation through births. An existing pair of individuals separated by a displacement $\boldsymbol{\xi}$ can be lost if either one of the individuals dies, which occurs at a rate $D_2(\boldsymbol{\xi}, t)$. Conversely, a new pair separated by $\boldsymbol{\xi}$ can be generated in two ways. First, if a pair already exists at displacement $\boldsymbol{\xi} + \boldsymbol{\xi}'$, one of these individuals can disperse a daughter organism at a displacement $\boldsymbol{\xi}'$, forming a new pair with displacement $\boldsymbol{\xi}$. This occurs at a rate $b\phi_D(\boldsymbol{\xi}')$. Second, a new pair at displacement $\boldsymbol{\xi}$ can be created when a single individual disperses an offspring at displacement $-\boldsymbol{\xi}$, occurring at a rate $b\phi_D(-\boldsymbol{\xi})$. Combining these possibilities, we write the time evolution of the second spatial moment as,

$$\frac{d}{dt} Z_2(\boldsymbol{\xi}, t) = -2D_2(\boldsymbol{\xi}, t)Z_2(\boldsymbol{\xi}, t) + 2b \int \phi_D(\boldsymbol{\xi}') Z_2(\boldsymbol{\xi} + \boldsymbol{\xi}', t) d\boldsymbol{\xi}' + 2b\phi_D(-\boldsymbol{\xi})Z_1(t). \quad (2.11)$$

The dynamics of the second moment still depend on the third moment through the definition of D_2 in (2.10), requiring a moment closure approximation to completely solve Eq. (2.11). Here, we employ the power-2 asymmetric closure:

$$Z_3(\boldsymbol{\xi}, \boldsymbol{\xi}', t) = \frac{\left(4Z_2(\boldsymbol{\xi}, t)Z_2(\boldsymbol{\xi}', t) + Z_2(\boldsymbol{\xi}, t)Z_2(\boldsymbol{\xi}' - \boldsymbol{\xi}, t) + Z_2(\boldsymbol{\xi}', t)Z_2(\boldsymbol{\xi}' - \boldsymbol{\xi}, t) - Z_1^4(t)\right)}{5Z_1(t)}, \quad (2.12)$$

which approximates the third moment in terms of the first two spatial moments [55, 58].

Moment closures approximating the third moment in terms of the first two moments inherently relies on two key assumptions. First, the third moment must be positive, as it represents triplet density and is calculated from the product of three non-negative densities [Eq. (2.6)]. Therefore, the closure approximation must also remain non-negative. The second assumption is the dynamical invariance under relabeling, implying that relabeling identical individuals should not alter the system dynamics [58]. Different closure methods balance these assumptions, with the power-2 closure we used in our computations offering an optimal trade-off between them. However, in certain parameter regimes, these assumptions may not hold, leading to notable discrepancies between IBM and SMD [58, 59]. Additionally, truncating the hierarchy of spatial moments at the second order may limit model accuracy for spatial structures with significant amounts of information in spatial moments

at higher orders. Nevertheless, many previous studies successfully implemented moment closures to approximate spatial patterns and population dynamics in interacting particle system [32, 60, 61].

2.3 Field equation for the biomass density field

Additionally, we can develop a coarse-grained equation for the biomass density field. This approximation is particularly useful when the spatial logistic model exhibits periodic spatial patterns. To derive this equation, we first discretize the two-dimensional square domain of lateral length L used in the IBM definition into m square cells of lateral length $dx = L/m$. Each cell can be labeled with a pair of indices, (i, j) where $i, j = 1, \dots, m$, represent the cell coordinates in the discrete grid.

In this discretized space, the system's state is given by the number of individuals in each grid cell $\mathbf{\Omega} \equiv \{N_{11}, N_{12}, \dots, N_{mm}\}$. At a given time t , the population is found in one of these states with a probability $P(\mathbf{\Omega}, t)$ that can be used to compute the expected number of individuals in a focal cell

$$\langle N_{ij} \rangle = \sum_{\mathbf{\Omega}} N_{ij} P(\mathbf{\Omega}, t), \quad (2.13)$$

where the average is over an ensemble of independent realizations of the individual-based stochastic dynamics. We can formally define the dynamics of this expected occupation number as

$$\frac{d\langle N_{ij} \rangle}{dt} = \sum_{\mathbf{\Omega}} N_{ij} \frac{\partial P(\mathbf{\Omega}, t)}{\partial t}, \quad (2.14)$$

where the time derivative of $P(\mathbf{\Omega}, t)$ will be given by a master equation of the form

$$\frac{\partial P(\mathbf{\Omega}, t)}{\partial t} = \sum_{\mathbf{\Omega}'} \mathcal{T}(\mathbf{\Omega}' \rightarrow \mathbf{\Omega}) P(\mathbf{\Omega}', t) - \mathcal{T}(\mathbf{\Omega} \rightarrow \mathbf{\Omega}') P(\mathbf{\Omega}, t) \quad (2.15)$$

where the sum in $\mathbf{\Omega}'$ runs over all possible states and \mathcal{T} are the transition rates between states and are given by the rules of the individual-based stochastic model. Because the probability of simultaneous births and deaths events is negligible, the IBM stochastic dynamics is a *one step process* [62]. In terms of the Master equation (2.15), this means that the transition rates \mathcal{T} between pairs of states that differ in more than one particle are all zero. With this condition and using step operators [63], we can write the Master equation as

$$\frac{\partial P(\mathbf{\Omega}, t)}{\partial t} = \sum_{kl} (E_{kl}^- - 1) \mathcal{T}(\mathbf{\Omega} \rightarrow \mathbf{\Omega}_{kl}^+) P(\mathbf{\Omega}, t) + (E_{kl}^+ - 1) \mathcal{T}(\mathbf{\Omega} \rightarrow \mathbf{\Omega}_{kl}^-) P(\mathbf{\Omega}, t), \quad (2.16)$$

where we have defined the up-down step operators such that

$$E_{ij}^{\pm}[f(\boldsymbol{\Omega})] = f[\{N_{11}, \dots, N_{ij} \pm 1, \dots, N_{mm}\}] \quad (2.17)$$

and the states $\boldsymbol{\Omega}_{kl}^{\pm}$ are identical to $\boldsymbol{\Omega}$ but have ± 1 individual in the kl -th element. To fully describe the stochastic dynamics, we need to define the transition rates,

$$\mathcal{T}(\boldsymbol{\Omega} \rightarrow \boldsymbol{\Omega}_{kl}^+) = \sum_{ij} b N_{ij} \phi_D(|\mathbf{x}_{ij} - \mathbf{x}_{kl}|) dx^2, \quad (2.18)$$

$$\mathcal{T}(\boldsymbol{\Omega} \rightarrow \boldsymbol{\Omega}_{kl}^-) = N_{kl} \left(d + g \sum_{ij} N_{ij} \phi_C(|\mathbf{x}_{ij} - \mathbf{x}_{kl}|) \right). \quad (2.19)$$

Inserting the Master equation (2.16) with the transition rates in Eqs. (2.18)-(2.19) into the definition for the time derivative of the mean number of particles in each spatial cell, Eq. (2.14), we obtain

$$\frac{d\langle N_{ij} \rangle}{dt} = b \sum_{kl} \phi_D(|\mathbf{x} - \mathbf{x}'|) dx^2 \langle N_{kl} \rangle - d \langle N_{ij} \rangle - g \sum_{kl} \phi_C(|\mathbf{x} - \mathbf{x}'|) \langle N_{ij} N_{kl} \rangle, \quad (2.20)$$

where we have used the constraint that $\langle N_{ij} \rangle \geq 0 \forall ij$ and thus the probability of states with a negative number of particles, and the transition rates into them, must be zero. Finally, defining a scaled density of individuals, $n(\mathbf{x}_{ij}) = N_{ij} g / b dx^2$, and time $\tau = bt$ we obtain a partial differential equation for a population density field

$$\frac{\partial \langle n \rangle}{\partial \tau}(\mathbf{x}, \tau) = \int \phi_D(|\mathbf{x} - \mathbf{x}'|) \langle n(\mathbf{x}') \rangle d\mathbf{x}' - \frac{d}{b} \langle n(\mathbf{x}) \rangle - \int \phi_C(|\mathbf{x} - \mathbf{x}'|) \langle n(\mathbf{x}) n(\mathbf{x}') \rangle d\mathbf{x}', \quad (2.21)$$

where we have omitted the time dependence on the right side. We now define the total number of plants in the population as $N = \int \langle n(\mathbf{x}) \rangle d\mathbf{x} = Z_1 \times L^2$. Under the mean-field condition, the total number of plants in the population is denoted by N_h . Notice that, similarly to what we obtained in the spatial moment dynamics equations in Section 2.2, Eq. (2.21) does not provide a closed description for the dynamics of the population density because it also includes its spatial covariance. We could write an equation for the dynamics of this spatial covariance and perform a moment closure approximation, as we did with the spatial moment dynamics equations. This approach is now much more complicated because the plant density is a field rather than a scalar quantity obtained from a spatial average. Therefore, we explore two alternative ways of treating these spatial correlations.

2.3.1 Mean-field approximation and the nonlocal Fisher KPP equation

The simplest and most common approximation to treat spatial correlations in Eq. (2.21) is to neglect the spatial covariance in the density field,

$$\text{Cov}(\mathbf{x}, \mathbf{x}') = \langle n(\mathbf{x})n(\mathbf{x}') \rangle - \langle n(\mathbf{x}) \rangle \langle n(\mathbf{x}') \rangle = 0 \quad (2.22)$$

which implies that

$$\langle n(\mathbf{x})n(\mathbf{x}') \rangle = \langle n(\mathbf{x}) \rangle \langle n(\mathbf{x}') \rangle. \quad (2.23)$$

Replacing Eq. (2.23) into (2.21), we obtain

$$\frac{\partial \langle n \rangle}{\partial \tau}(\mathbf{x}, \tau) = \int \phi_D(|\mathbf{x} - \mathbf{x}'|) \langle n(\mathbf{x}') \rangle d\mathbf{x}' - \frac{d}{b} \langle n(\mathbf{x}) \rangle - \langle n(\mathbf{x}) \rangle \int \phi_C(|\mathbf{x} - \mathbf{x}'|) \langle n(\mathbf{x}') \rangle d\mathbf{x}', \quad (2.24)$$

that is an extension of the Fisher-Kolmogorov equation with nonlocalities in the competition and the growth terms. Defining a change of variables $\mathbf{y} \equiv \mathbf{x} - \mathbf{x}'$ in the first integral of Eq. (2.24) and expanding the density $\langle n(\mathbf{x} - \mathbf{y}) \rangle$ about \mathbf{x} as a Taylor expansion up to second order, Eq. (2.24) reduces to

$$\frac{\partial \langle n \rangle}{\partial \tau}(\mathbf{x}, \tau) = \langle n(\mathbf{x}) \rangle - \frac{d}{b} \langle n(\mathbf{x}) \rangle - \langle n(\mathbf{x}) \rangle \int \phi_C(|\mathbf{x} - \mathbf{x}'|) \langle n(\mathbf{x}') \rangle d\mathbf{x}' + \frac{\omega_2}{2} \frac{\partial^2}{\partial x^2} \langle n(\mathbf{x}) \rangle, \quad (2.25)$$

which is the nonlocal Fisher KPP equation with a diffusion coefficient defined by the reproduction rate (here absorbed in the scaled time) and the second moment of the dispersal kernel [64]. However, because we are interested in how long-range dispersal influences spatial patterns, we will retain the nonlocal dispersal term.

2.3.2 Beyond mean-field: introducing the effect of spatial covariances

Because Eq. (2.21) is isotropic and homogeneous, we propose an ansatz for the covariance of the form

$$\text{Cov}(\mathbf{x}, \mathbf{x}') = \langle n(\mathbf{x}) \rangle \langle n(\mathbf{x}') \rangle f(|\mathbf{x} - \mathbf{x}'|), \quad (2.26)$$

where $f(|\mathbf{x} - \mathbf{x}'|)$ is such that its modulus decays with its argument. In particular, to account for the fact that the spatial correlations of the density field go to zero when two points are very far from each other, $f(r) \rightarrow 0$ as $r \rightarrow \infty$ (where $r \equiv |\mathbf{x} - \mathbf{x}'|$). Inserting this ansatz into the definition of the covariance in Eq. (2.22), we can write the second moment of the density field as,

$$\langle n(\mathbf{x})n(\mathbf{x}') \rangle = \langle n(\mathbf{x}) \rangle \langle n(\mathbf{x}') \rangle [1 + f(|\mathbf{x} - \mathbf{x}'|)], \quad (2.27)$$

that we can insert into Eq. (2.21) to obtain

$$\frac{\partial \langle n \rangle}{\partial \tau}(\mathbf{x}, \tau) = \int \phi_D(|\mathbf{x} - \mathbf{x}'|) \langle n(\mathbf{x}') \rangle d\mathbf{x}' - \frac{d}{b} \langle n(\mathbf{x}) \rangle - \langle n(\mathbf{x}) \rangle \int \phi_C(|\mathbf{x} - \mathbf{x}'|) (1 + f(|\mathbf{x} - \mathbf{x}'|)) \langle n(\mathbf{x}') \rangle d\mathbf{x}'. \quad (2.28)$$

Provided that we know the form of the function f , this equation fully describes the dynamics of the biomass density field, replacing the spatial correlations $\langle n(\mathbf{x})n(\mathbf{x}') \rangle$ by an effective competition kernel that includes the ansatz function f .

To obtain an expression for this function f , we average Eq. (2.26) over space

$$\int \text{Cov}(\mathbf{x}, \mathbf{x} + \mathbf{x}') d\mathbf{x} = f(|\mathbf{x}'|) \int \langle n(\mathbf{x}) \rangle \langle n(\mathbf{x} + \mathbf{x}') \rangle d\mathbf{x}, \quad (2.29)$$

from where we can write f as a function of different features of the spatial pattern of population density,

$$f(|\mathbf{x}'|) = \frac{\int \text{Cov}(\mathbf{x}, \mathbf{x} + \mathbf{x}') d\mathbf{x}}{\int \langle n(\mathbf{x}) \rangle \langle n(\mathbf{x} + \mathbf{x}') \rangle d\mathbf{x}}. \quad (2.30)$$

All the quantities on the right side of Eq. (2.30) can be computed from IBM simulations. Alternatively, these quantities can also be obtained using the spatial moment dynamics (SMD) equations, which is computationally more efficient and makes it possible to have a closed dynamical equation for the vegetation density field without performing IBM simulations. Using the definitions of the spatial moments, we can rewrite (2.30) as,

$$f(|\mathbf{x} - \mathbf{x}'|) = \frac{Z_2(|\mathbf{x} - \mathbf{x}'|)}{Z_1^2} - 1, \quad (2.31)$$

where we have used the pattern isotropy to write the dependence of the second spatial moment on the distance between two points explicitly. Using this relationship, we can describe the dynamics of the biomass density field using a system of two coupled equations: we use the equation for the second spatial moment to determine the density correlations and the function f , which we then insert in Eq. (2.28), to obtain the density field. In the next sections, we compare the accuracy of all these approximations to reproduce the total biomass density and pattern structure obtained in simulations of the stochastic IBM.

3 Results and Discussion

3.1 Spatial patterns in the discrete model

We first review the behavior of the spatially explicit spatial logistic model presented in Section 2.1 using a Gaussian competition kernel with standard deviation r_c [30, 36] and a Gaussian dispersal

kernel with standard deviation s . Holding the demographic parameters, b , d , and g constant, the spatial correlations in the distribution of organisms are controlled by the dispersal and competition range.

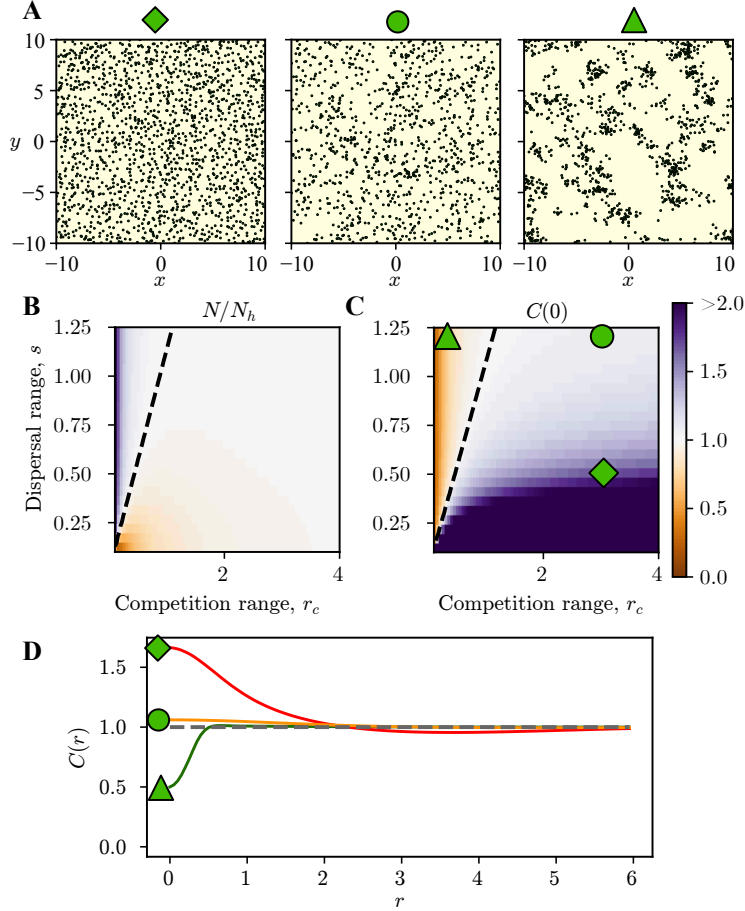


Figure 1: IBM analysis using a Gaussian competition kernel. A) Snapshots of spatial patterns from IBM simulations. From left to right: segregated, uniform, and clustered patterns, denoted by diamond, circle, and triangle shapes, respectively. B) Total number of plants normalized by the homogenous (mean-field) expectation, $N/N_h = (b - d)/g$. C) Radial correlation function at displacement zero $C(0)$ [36] as a function of the dispersal and competition ranges, s and r_c respectively. In both these heatmaps, we plot the steady-state values of N/N_h and $C(0)$, respectively, and depict time-averaged values computed up to $t = 250$. D) Radial correlation function, $C(r)$, as a function of the separation distance, r , for three combinations of s and r_c . These parameter combinations are indicated by the coordinates of the green symbols in the heat map and correspond to the respective patterns in A). The gray dashed line represents $C(r) = 1$.

Previous work has identified four possible types of spatial patterns depending on how these two scales compare to each other [36]. When both ranges are large, the dynamics are effectively non-spatial with a uniform spatial pattern, and the IBM converges to the classical logistic model. However, when the dispersal scale decreases, while keeping competition long-ranged, individuals

tend to clump together forming a clustered spatial pattern. This scenario leads to smaller population sizes than in the non-spatial case. Likewise, when the competition range decreases while keeping dispersal long-range, individuals tend to overdisperse, forming a segregated pattern, which increases the total population size. We show the spatial snapshot of these different possible patterns in Fig. 1A. Finally, when both competition and dispersal are short-range, newborns cannot escape from competition with their ancestors and the population goes extinct. We recover these results integrating the SMD approximation in Eqs. (2.9)-(2.11) with the moment closure in Eq. (2.12) (Fig. 1B, C). In none of the scenarios discussed above, however, the spatial patterns are periodic (see radial correlation functions in Fig. 1D). Therefore, any of the continuous approximations we derived for the plant biomass density will return a homogeneous solution.

To investigate whether regular patterns exist in our model, we solved the SMD equations using a top-hat kernel as defined in Eq. (2.3) and compared these predictions with results from simulations of the discrete IBM. The IBM simulations show the emergence of regular patterns when the dispersal range is short and the competition range long (Fig. 2). This result is in good agreement with previous work using various nonlocal extensions of the Fisher KPP equation with top-hat competition kernels [46, 52]. We find that the SMD equations accurately predict the value of the radial correlation function at pairwise distance zero (top panels in Fig. 3B, C), which is a proxy for local crowding. The SMD equations, however, predict less accurately the total number of plants in the population. Specifically, when the competition range is large, and the dispersal range is short, the SMD equations underestimate the total population size resulting from the IBM simulations (Fig. 3B, C).

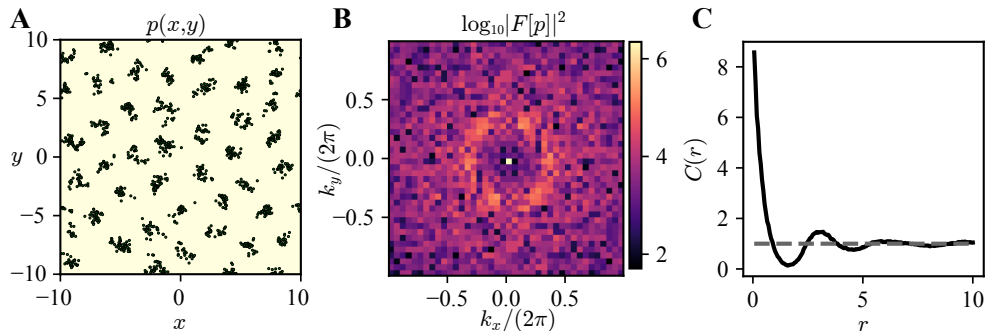


Figure 2: A) Long-time pattern snapshot with dispersal range $s = 0.15$ and competition range $r_c = 2.2$ (inside the region of high aggregation (labeled with the diamond marker) in the $C(0)$ heatmaps in Fig. 3). B) Fourier transform of the pattern snapshot. C) Radial correlation function, $C(r)$, of the pattern snapshot.

This discrepancy in the total population size comes from the inaccurate prediction of the full radial correlation function provided by the SMD equations. In particular, SMD does not fully capture the amplitude of the oscillations in the radial correlation functions measured from IBM simulations (rightmost panel in the bottom row of Fig. 3B, C). This amplitude, especially when

the radial correlation function becomes less than unity, is critical to determine how larger the population size grows when regular patterns form. More smaller the values of $C(r)$ indicate that the regions between clusters are less populated, which favors the growth of more individuals within each aggregate [47].

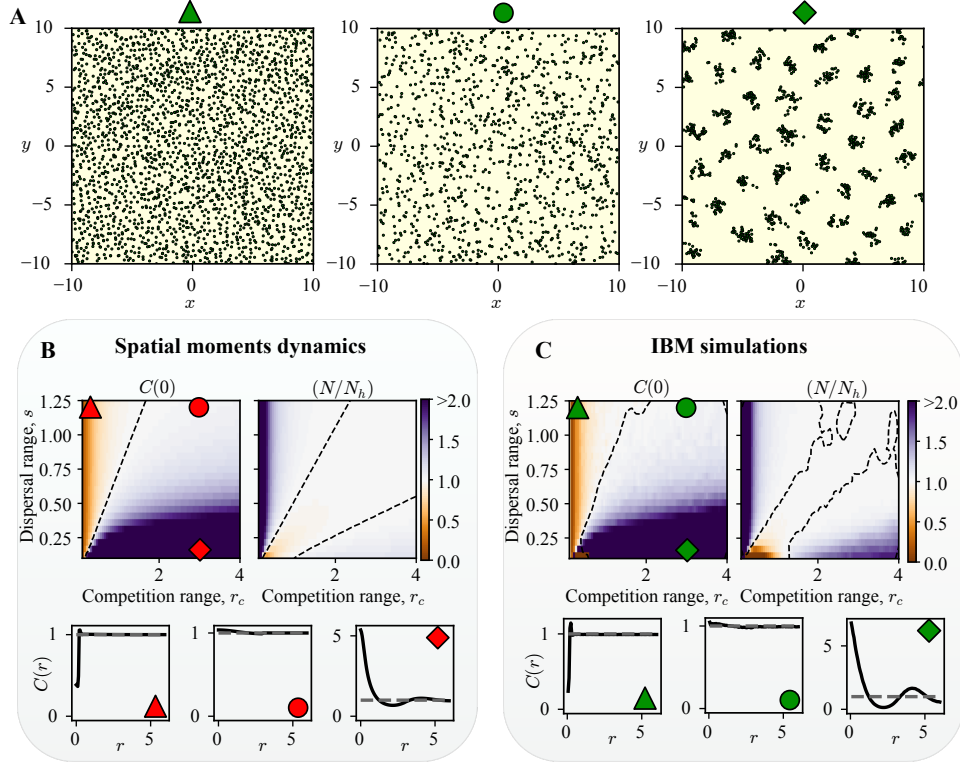


Figure 3: IBM analysis using a top-hat competition kernel. A) Snapshots of the spatial patterns from IBM simulations. From left to right: segregated, uniform, and regular aggregated patterns, denoted by triangle, circle, and diamond shapes, respectively. B) Top panels: SMD predictions for the radial correlation function at zero displacement, $C(0)$, and the total number of individuals normalized by the homogenous expectation, N/N_h . In both these heatmaps, we plot the steady-state values of $C(0)$ and N/N_h , respectively, which we computed using time-averaged values up to $t = 250$. The bottom three panels in B) show the radial correlation function, $C(r)$, as a function of the separation distance r for three specific combinations of s and r_c . These parameter combinations are indicated by the coordinates of the red symbols in the heat maps and correspond to the respective patterns in A). The gray dashed lines represent $C(0) = 1$. C) Same as in B) but computed directly from stochastic IBM simulations instead of SMD predictions.

3.2 Pattern formation in the field equation

To test the accuracy of the field equation in predicting the behavior of the individual-based simulations, we performed a linear stability analysis around the non-trivial homogenous solution to obtain

the onset of pattern formation. Doing this analysis on the coupled system of equations for the second spatial moment Z_2 and the density field $\langle n \rangle$ is very challenging because the equation for Z_2 is inhomogeneous (it depends explicitly on space) and thus does not have any homogeneous equilibrium apart from the vanishing density field for which $Z_2 = 0$ too. Therefore, instead of working with the full system of coupled equations, we use the results from the SMD numerical simulation and assume that $Z_2 = (1 + f)Z_1^2$ is a fixed point of $\dot{Z}_2 = 0$. Inserting this solution into the equation for $\langle n \rangle$, we obtain the density equilibrium

$$\langle n \rangle_h = \frac{1 - \frac{d}{b}}{1 + \int \phi_C(|\mathbf{x}'|)f(|\mathbf{x}'|)d\mathbf{x}'}. \quad (3.1)$$

We can perform a linear stability analysis of this equilibrium for small spatiotemporal perturbations, considering that Z_2 (and hence f) is given. We insert the expressions $\langle n(\mathbf{x})n(\mathbf{x}') \rangle = \langle n(\mathbf{x}) \rangle \langle n(\mathbf{x}') \rangle (1 + f(\mathbf{x} - \mathbf{x}'))$ and $\langle n(\mathbf{x}) \rangle = \langle n \rangle_h + \Delta n e^{i\mathbf{k} \cdot \mathbf{x} + \lambda(\mathbf{k})t}$ in Eq. (2.21), where Δn is the amplitude of the spatiotemporal perturbation. Then, linearizing in Δn , we obtain an equation describing the linear dynamics around the equilibrium. For more details of this technique applied to ecosystem models, see Ref. [65]. This calculation provides the linear growth rate of the density Fourier modes

$$\lambda(\mathbf{k}) = F[\phi_D](\mathbf{k}) - \langle n \rangle_h F[\phi_C(1 + f)](\mathbf{k}) - \left(\frac{d}{b} + \langle n \rangle_h \int \phi_C(|\mathbf{x}'|)f(|\mathbf{x}'|)d\mathbf{x}' \right), \quad (3.2)$$

where $F[\]$ indicates a Fourier transform operation. The onset of pattern formation is defined by the parameter values such that $\lambda(\mathbf{k}_c) = 0$, where \mathbf{k}_c is the non-zero Fourier mode at which the perturbation growth rate is maximum. Therefore, we can define the region where patterns might exist by scanning the (s, r_c) parameter space and testing for the pattern onset condition.

To quantify how accurately this linear stability analysis predicts the region of the IBM in which regular patterns form, we need to measure regularity in the stochastic patterns obtained from the discrete simulations. We introduce two different Fourier-based metrics, a first one based on comparing the distribution of Fourier spectra generated by simulated and random patterns, and a second one based on how strongly the pattern wavenumber (maximum of the pattern power spectrum) contributes to the total power of the pattern spectrum.

The first metric, \mathcal{R} compares the spatial properties of IBM simulated patterns with those of completely spatial random distributions of individuals. To this end, we first generated an ensemble of spatial patterns for each parameter combination using IBM simulations and obtained their radial power spectra as the squared magnitude of the pattern Fourier transform averaged over the angular degree of freedom. Then, we obtained the completely spatial random counterpart of each simulated

pattern by randomizing the individual locations to be uniformly distributed within the simulation domain and computed the radial power spectra of this random pattern. Lastly, we computed the average of both the simulated (50 snapshots, 10 snapshots for 5 IBM realizations) and random (500 realizations, 100 for the 5 IBM obtained number of particles) power spectra and the confidence interval as the 2.5%-97.5% interpercentile range. We define the regularity \mathcal{R} as the distance between the 2.5% percentile of the IBM radial power spectra distribution and the 97.5% percentile of its random counterpart, evaluated at the pattern wavenumber (i.e., the peak of the IBM radial power spectrum). In Fig. 4, we show two examples in which this metric returns regular and non-regular patterns). We define patterns as *significantly* regular when they have a regularity metric, \mathcal{R} , greater than zero ($\mathcal{R} > 0$, the confidence bands do not overlap at the peak). On the contrary, we define patterns as *not significantly* regular when they have a negative regularity metric ($\mathcal{R} < 0$, the confidence bands overlap at the peak) despite them exhibiting a peak in the power spectrum. The reason is that, for $\mathcal{R} < 0$, there is a non-negligible chance that a random pattern could exhibit the same peak in the Fourier power spectrum as a corresponding IBM simulation.

The second metric quantifies how strong is the periodicity in the IBM simulated patterns measuring the amplitude of the characteristic wavenumber (the wavenumber at which the radial power spectrum is maximum) compared to the total power, computed as the integral of the radial power spectrum across the entire range of wavenumber. The reason is that, a perfectly linear periodic pattern (a sine function, for example) has all the power in the peak of the spectrum, and a distribution with no periodicity shows a flat power spectrum.

Both metrics identify that regular patterns form when the dispersal range is short and the competition range is large (bottom right corner in Fig. 5). To compare these results with the predictions of density equations, both mean-field and accounting for spatial correlations, we evaluated the pattern formation onset derived from Eq. (3.2) for the different approximations of $f(\mathbf{r})$ quantifying the density correlations. To perform this calculation, we imposed the Turing instability condition, $\lambda(\mathbf{k}_c) = 0$ and $\nabla\lambda(\mathbf{k}_c) = 0$, in Eq. (3.2) for the three different approximations of the $f(\mathbf{r})$ function: $f = 0$, which corresponds to the mean-field approximation neglecting spatial correlations, $f(\mathbf{r})$ obtained by evaluating the spatial covariances in Eq. (2.30) using IBM simulations, and $f(\mathbf{r})$ obtained from the SMD approximation as defined by Eq. (2.31). The mean-field approximation (gray line in Fig. 5) underestimates the region of the (s, r_c) parameter space where periodic patterns exist. However, accounting for spatial correlations, either using the SMD equations or IBM simulations, provides a much better agreement with the results of the discrete model (cyan symbols and red dashed line in Fig. 5). Additionally, the agreement between the corrected PDE and the IBM simulations is much better when regularity in the discrete patterns is measured using the relative amplitude of the pattern wavenumber (second metric). This metric provides a much more robust

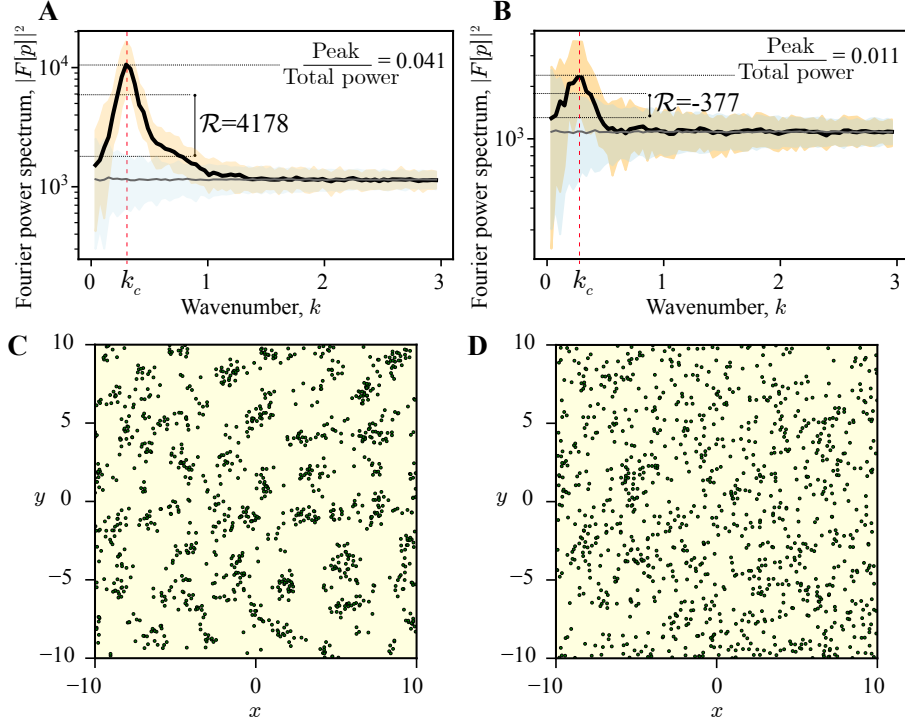


Figure 4: Power spectra distributions obtained from IBM simulations (black line with orange envelopes indicating the 2.5%-97.5% interpercentile range), indicating the corresponding regularity metric and the relative power of the characteristic wavenumber, and spatially random point patterns (gray line with blue envelopes indicating the 2.5%-97.5% interpercentile range). A) $\mathcal{R} > 0$ at the pattern wavenumber, thus, IBM patterns are significantly regular. B) $\mathcal{R} < 0$, thus, IBM patterns are not significantly regular. C and D show corresponding snapshots of the IBM simulations. Parameters used were $s = 0.3$ and $r_c = 2.2$ for panels A and C. Parameters $s = 0.65$ and $r_c = 2.2$ for panels B and D.

measurement of regularity because it does not rely on any statistical modeling assumption. The first metric we introduced \mathcal{R} , however, quantifies regularity as a statistically significant difference between random patterns and those resulting from the IBM simulation, which makes the definition of regularity sensitive to both the number of pattern realizations we used to construct the statistical ensembles and the percentiles used to define the difference between power spectra distributions. As a result, the transition from regular to non-regular patterns, indicated by the white region in Fig. 5a, will vary depending on how we choose these quantities.

4 Conclusions

We investigated the spatial patterns that form in a spatially explicit IBM logistic model with nonlocal dispersal and intraspecific competition using both a Gaussian and top-hat competition kernel. Combining numerical simulations of the discrete model and a spatial moment dynamics

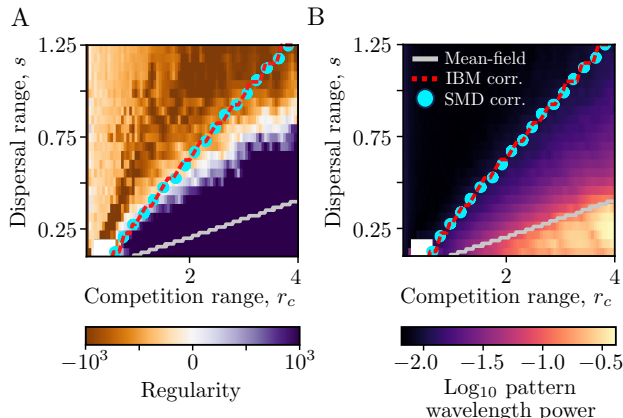


Figure 5: Validation of how the different PDE approximations predict regular patterns. A) Regularity is quantified by measuring statistically significant differences between IBM simulated and random patterns (see main text for a detailed description of how the metric is computed). B) Regularity is measured by the relative amplitude of the pattern wavenumber (i.e., ratio between the power of the wavenumber with maximum power and the total power). Curves in both panels show the onset of pattern formation obtained from the linear stability analysis of the density equation. Each curve corresponds to a different approximation to treat the spatial correlations as indicated in the legend in panel (B).

approximation, we found that, for top-hat competition kernels, the population might exhibit periodic patterns with aggregates of individuals forming a hexagonal lattice [46]. This type of pattern is not present when long-range competition is modeled using a Gaussian kernel [36], this fact is due to our IBM rules, and can be seen mathematically by inserting a Gaussian kernel in Eq. (3.2) for $f = 0$ (mean-field approximation); however, there are models for which a Gaussian competition kernel can produce patterns, highlighting that the issue of the general conditions for pattern formation is still debated [33]. Interestingly, the emergence of these regular patterns also affects the system productivity, allowing for larger population sizes even in conditions where local individual crowding is high [52].

Next, we looked at how accurately a field equation for the biomass density, obtained by upscaling the individual-based dynamics, reproduced the existence of regular patterns. We found that the standard mean-field approximation, which neglects spatial covariates in the density field, does not fully capture the region of the parameter space with regular patterns. To improve this prediction, we developed a novel approximation that uses spatial-moment dynamics equations to introduce the effect of spatial covariates in the density field. This corrected density equation accurately reproduces the region with regular patterns, offering a new avenue to study pattern formation in sessile organisms using continuous, density-based models beyond mean-field approximations.

For ecological modeling applications in general and particularly in the case of vegetation patterns, individual-based models provide a robust framework with a high degree of accuracy in simulating

individual-level processes and interactions, capturing dynamics down to the resolution of single plants. Consequently, these models are very effective for understanding the fine-scale mechanisms driving vegetation pattern formation. However, the computational overhead in simulating these IBMs becomes prohibitively expensive when the system size is large or longer temporal scales are considered, limiting their practical applicability. Density-based models, on the other hand, are computationally very efficient and often amenable to analytical exploration. However, these models assume that interactions are, to some extent, well-mixed, which lead to inaccuracies when trying to determine in which conditions spatial patterns form in vegetation systems. The spatial moment model provides a middle ground, balancing computational feasibility with the ability to incorporate spatial structure explicitly. This approach retains key insights from IBMs regarding spatial patterns and spatially explicit interactions while remaining computationally tractable for larger-scale analyses.

Acknowledgments

This work was partially funded by the Center of Advanced Systems Understanding (CASUS), which is financed by Germany's Federal Ministry of Education and Research (BMBF) and by the Saxon Ministry for Science, Culture and Tourism (SMWK) with tax funds on the basis of the budget approved by the Saxon State Parliament. RMG was supported by FAPESP through grant ICTP-SAIFR 2021/14335-0. RM was supported by CNPq through grant 140096/2021-3 and CAPES - Finance Code 001.

References

- [1] Pringle RM, Tarnita CE. Spatial Self-Organization of Ecosystems: Integrating Multiple Mechanisms of Regular-Pattern Formation. *Annual Review of Entomology*. 2017;62(1):359-77.
- [2] Lee ED, Kempes CP, West GB. Growth, death, and resource competition in sessile organisms. *Proceedings of the National Academy of Sciences of the United States of America*. 2021;118(15). ISBN: 2020424118.
- [3] Rietkerk M, van de Koppel J. Regular pattern formation in real ecosystems. *Trends in ecology & evolution*. 2008 Mar;23(3):169-75. Publisher: Elsevier Science Publishers. Available from: <http://linkinghub.elsevier.com/retrieve/pii/S0169534708000281>.
- [4] Martinez-Garcia R, Tarnita CE, Bonachela JA. Self-organized patterns in ecological systems: from microbial colonies to landscapes. *Emerging Topics in Life Sciences*. 2022;6(3):245-58.

Available from: <https://portlandpress.com/emergtoplifesci/article-abstract/6/3/245/231411/Spatial-patterns-in-ecological-systems-from?redirectedFrom=fulltext>.

- [5] Tarnita CE. Self-organization in spatial ecology. *Current Biology*. 2024 Oct;34(20):R965-70. Available from: <https://linkinghub.elsevier.com/retrieve/pii/S0960982224012430>.
- [6] Rohani P, Lewis TJ, Grünbaum D, Ruxton GD. Spatial self-organization in ecology: Pretty patterns or robust reality? *Trends in Ecology and Evolution*. 1997;12(2):70-4.
- [7] Dong X, Fisher SG. Ecosystem spatial self-organization: Free order for nothing? *Ecological Complexity*. 2019 Apr;38:24-30. Available from: <https://linkinghub.elsevier.com/retrieve/pii/S1476945X18301508>.
- [8] Rietkerk M, Bastiaansen R, Banerjee S, van de Koppel J, Baudena M, Doelman A. Evasion of tipping in complex systems through spatial pattern formation. *Science*. 2021;374(6564):eabj0359.
- [9] Kéfi S, Génin A, Garcia-Mayor A, Guirado E, Cabral JS, Berdugo M, et al. Self-organization as a mechanism of resilience in dryland ecosystems. *Proceedings of the National Academy of Sciences*. 2024;121(6):e2305153121.
- [10] Rietkerk M, Boerlijst MC, van Langevelde F, HilleRisLambers R, de Koppel Jv, Kumar L, et al. Self-Organization of Vegetation in Arid Ecosystems. *The American Naturalist*. 2002 Oct;160(4):524-30. ISBN: 0003-0147.
- [11] Lefever R, Lejeune O. On the origin of tiger bush. *Bulletin of Mathematical biology*. 1997;59:263-94.
- [12] Deblauwe V, Couteron P, Lejeune O, Bogaert J, Barbier N. Environmental modulation of self-organized periodic vegetation patterns in Sudan. *Ecography*. 2011;34(6):990-1001.
- [13] Clerc MG, Echeverría-Alar S, Tlidi M. Localised labyrinthine patterns in ecosystems. *Scientific reports*. 2021;11(1):18331.
- [14] Guirado E, Delgado-Baquerizo M, Benito BM, Molina-Pardo JL, Berdugo M, Martínez-Valderrama J, et al. The global biogeography and environmental drivers of fairy circles. *Proceedings of the National Academy of Sciences*. 2023;120(40):e2304032120.
- [15] Gandhi P, Werner L, Iams S, Gowda K, Silber M. A topographic mechanism for arcing of dryland vegetation bands. *Journal of The Royal Society Interface*. 2018;15(147):20180508. Available from: <http://dx.doi.org/10.1098/rsif.2018>.

0508Electronicsupplementarymaterialisavailableonlineat<https://dx.doi.org/10.6084/m9.figshare.c.4238546>.

- [16] Gowda K, Iams S, Silber M. Signatures of human impact on self-organized vegetation in the Horn of Africa. *Scientific Reports*. 2018;8(1):1-8. ArXiv: 1705.05308 Publisher: Springer US. Available from: <http://dx.doi.org/10.1038/s41598-018-22075-5>.
- [17] Siteur K, Liu QX, Rottschäfer V, Heide Tvd, Rietkerk M, Doelman A, et al. Phase-separation physics underlies a new theory for the resilience of patchy ecosystems. *Proceedings of the National Academy of Sciences*. 2023;120(2):e2202683120. ISBN: 1211925110. Available from: <http://www.pnas.org/lookup/suppl/doi:10.1073/pnas.2216830120/-/DCSupplemental>.<https://doi.org/10.1073/pnas.2216830120>.
- [18] Pinto-Ramos D, Clerc MG, Tlidi M. Topological defects law for migrating banded vegetation patterns in arid climates. *Science Advances*. 2023;9(31):1-12.
- [19] Hidalgo-Ogalde B, Pinto-Ramos D, Clerc MG, Tlidi M. Nonreciprocal feedback induces migrating oblique and horizontal banded vegetation patterns in hyperarid landscapes. *Scientific reports*. 2024;14(1):14635.
- [20] Couteron P, Lejeune O. Periodic spotted patterns in semi-arid vegetation explained by a propagation-inhibition model. *Journal of Ecology*. 2001 Aug;89(4):616-28. Available from: <https://besjournals.onlinelibrary.wiley.com/doi/10.1046/j.0022-0477.2001.00588.x>.
- [21] Bastiaansen R, Jaïbi O, Deblauwe V, Eppinga MB, Siteur K, Siero E, et al. Multistability of model and real dryland ecosystems through spatial self-organization. *Proceedings of the National Academy of Sciences*. 2018 Oct;115(44):11256-61. Available from: <http://www.pnas.org/lookup/doi/10.1073/pnas.1804771115>.
- [22] Veldhuis MP, Martinez-Garcia R, Deblauwe V, Dakos V. Remotely-sensed slowing down in spatially patterned dryland ecosystems. *Ecography*. 2022;10:e06139.
- [23] Lejeune O, Tlidi M. A model for the explanation of vegetation stripes (tiger bush). *Journal of Vegetation Science*. 1999 Apr;10(2):201-8. Publisher: Blackwell Publishing Ltd. Available from: <http://dx.doi.org/10.2307/3237141>.
- [24] Meron E, Gilad E, Von Hardenberg J, Shachak M, Zarmi Y. Vegetation patterns along a rainfall gradient. *Chaos, Solitons and Fractals*. 2004;19(2):367-76. ISBN: 0960-0779.

- [25] Kealy BJ, Wollkind DJ. A Nonlinear Stability Analysis of Vegetative Turing Pattern Formation for an Interaction–Diffusion Plant-Surface Water Model System in an Arid Flat Environment. *Bulletin of Mathematical Biology*. 2012 Apr;74(4):803-33.
- [26] Martinez-Garcia R, Calabrese JM, Hernández-García E, López C. Vegetation pattern formation in semiarid systems without facilitative mechanisms. *Geophysical Research Letters*. 2013;40:6143-7.
- [27] Pinto-Ramos D, Clerc MG, Makhoute A, Tlidi M. Vegetation clustering and self-organization in inhomogeneous environments. *arXiv*. 2024 Jun. 2406.12581. Available from: <http://arxiv.org/abs/2406.12581>.
- [28] Bolker BM, Pacala SW. Spatial moment equations for plant competition: understanding spatial strategies and the advantages of short dispersal. *The American Naturalist*. 1999;153(6):575-602.
- [29] Wiegand T, Wang X, Anderson-Teixeira KJ, Bourg NA, Cao M, Ci X, et al. Consequences of spatial patterns for coexistence in species-rich plant communities. *Nature Ecology & Evolution*. 2021;5(7):965-73.
- [30] Bolker BM, Pacala SW. Using moment equations to understand stochastically driven spatial pattern formation in ecological systems. *Theoretical Population Biology*. 1997;52(3):179-97.
- [31] Plank MJ, Law R. Spatial Point Processes and Moment Dynamics in the Life Sciences: A Parsimonious Derivation and Some Extensions. *Bulletin of Mathematical Biology*. 2015 Apr;77(4):586-613. Available from: <http://link.springer.com/10.1007/s11538-014-0018-8>.
- [32] Surendran A, Plank MJ, Simpson MJ. Population dynamics with spatial structure and an Allee effect. *Proceedings of the Royal Society A: Mathematical, Physical and Engineering Sciences*. 2020;476:1-19.
- [33] Martinez-Garcia R, Cabal C, Calabrese JM, Hernández-García E, Tarnita CE, López C, et al. Integrating theory and experiments to link local mechanisms and ecosystem-level consequences of vegetation patterns in drylands. *Chaos, Solitons & Fractals*. 2023;166:112881.
- [34] Borgogno F, D’Odorico P, Laio F, Ridolfi L. Mathematical models of vegetation pattern formation in ecohydrology. *Reviews of Geophysics*. 2009;47(1). Available from: <http://dx.doi.org/10.1029/2007RG000256>.
- [35] Zelnik YR, Uecker H, Feudel U, Meron E. Desertification by front propagation? *Journal of Theoretical Biology*. 2017;418:27-35.

- [36] Law R, Murrell DJ, Dieckmann U. Population Growth in Space and Time : Spatial Logistic Equations. *Ecology*. 2003;84(1):252-62.
- [37] Sheffer E, Yizhaq H, Meron E. Emerged or imposed: a theory on the role of physical templates and self-organisation for vegetation patchiness. *Ecology Letters*. 2012.
- [38] Yizhaq H, Sela S, Svoray T, Assouline S, Bel G. Effects of heterogeneous soil-water diffusivity on vegetation pattern formation. *Water Resources Research*. 2014.
- [39] Echeverría-Alar S, Pinto-Ramos D, Tlidi M, Clerc M. Effect of heterogeneous environmental conditions on labyrinthine vegetation patterns. *Physical Review E*. 2023;107(5):054219.
- [40] Pinto-Ramos D, Echeverría-Alar S, Clerc MG, Tlidi M. Vegetation covers phase separation in inhomogeneous environments. *Chaos, Solitons & Fractals*. 2022;163:112518.
- [41] Butler T, Goldenfeld N. Robust ecological pattern formation induced by demographic noise. *Physical Review E*. 2009 Sep;80(3):030902. Publisher: American Physical Society. Available from: <http://link.aps.org/doi/10.1103/PhysRevE.80.030902>.
- [42] Martinez-Garcia R, Calabrese JM, López C. Spatial patterns in mesic savannas: The local facilitation limit and the role of demographic stochasticity. *Journal of Theoretical Biology*. 2013 Jun;333(0):156-65. ArXiv: 1209.5178v4 Publisher: Elsevier. Available from: <http://dx.doi.org/10.1016/j.jtbi.2013.05.024>.
- [43] Da Silva LA, Colombo EH, Anteneodo C. Effect of environment fluctuations on pattern formation of single species. *Physical Review E - Statistical, Nonlinear, and Soft Matter Physics*. 2014;90(1):1-8.
- [44] Karig D, Martini KM, Lu T, DeLateur NA, Goldenfeld N, Weiss R. Stochastic Turing patterns in a synthetic bacterial population. *Proceedings of the National Academy of Sciences*. 2018:201720770. ArXiv: 1408.1149 ISBN: 1720770115. Available from: <http://www.pnas.org/lookup/doi/10.1073/pnas.1720770115>.
- [45] Razo MJd, Lamma T, Merbis W. Field theories and quantum methods for stochastic reaction-diffusion systems. arXiv; 2024. ArXiv:2409.13377 [cond-mat]. Available from: <http://arxiv.org/abs/2409.13377>.
- [46] López C, Hernández-García E. Fluctuations impact on a pattern-forming model of population dynamics with non-local interactions. *Physica D: Nonlinear Phenomena*. 2004.

- [47] Jorge DCP, Martinez-Garcia R. Demographic effects of aggregation in the presence of a component Allee effect. *Journal Royal Society Interface*. 2024 Jun;21:20240042. Available from: <https://royalsocietypublishing.org/doi/10.1098/rsif.2024.0042>.
- [48] Meron E, Bennett JJR, Fernandez-Oto C, Tzuk O, Zelnik YR, Grafi G. Continuum Modeling of Discrete Plant Communities: Why Does It Work and Why Is It Advantageous? *Mathematics*. 2019;7(10):987.
- [49] Rogers HS, Beckman NG, Hartig F, Johnson JS, Pufal G, Shea K, et al. The Total Dispersal Kernel: A Review and Future Directions. *AoB PLANTS*. 2019 Sep;11(5):plz042.
- [50] Bullock JM, Mallada González L, Tamme R, Götzenberger L, White SM, Pärtel M, et al. A Synthesis of Empirical Plant Dispersal Kernels. *Journal of Ecology*. 2017;105(1):6-19.
- [51] Surendran A, Plank MJ, Simpson MJ. Small-scale spatial structure affects predator-prey dynamics and coexistence. *Theoretical Ecology*. 2020;13:537-50.
- [52] Silvano NO, Valeriano J, Hernández-García E, López C, Martinez-Garcia R. Shear and transport in a flow environment determine spatial patterns and population dynamics in a model of nonlocal ecological competition. *arXiv*. 2024 Sep. 2409.04268. Available from: <http://arxiv.org/abs/2409.04268>.
- [53] Hirsch BT, Visser MD, Kays R, Jansen PA. Quantifying seed dispersal kernels from truncated seed-tracking data. *Methods in Ecology and Evolution*. 2012;3(3):595-602. Available from: <https://besjournals.onlinelibrary.wiley.com/doi/abs/10.1111/j.2041-210X.2011.00183.x>.
- [54] Cabal C, Martínez-García R, Aguilar A, Valladares F, Pacala SW. The exploitative segregation of plant roots. *Science*. 2020;370(6521):1197-9. Available from: <https://www.science.org/doi/abs/10.1126/science.aba9877>.
- [55] Surendran A. Stochastic and continuum descriptions of population dynamics with spatial structure [PhD thesis]. Queensland University of Technology; 2021. Available from: <https://eprints.qut.edu.au/207574/>.
- [56] Surendran A, Plank MJ, Simpson MJ. Spatial moment description of birth–death–movement processes incorporating the effects of crowding and obstacles. *Bulletin of Mathematical Biology*. 2018;80:2828-55.
- [57] Surendran A, Plank MJ, Simpson MJ. Spatial structure arising from chase-escape interactions with crowding. *Scientific Reports*. 2019;9:14988.

- [58] Murrell DJ, Dieckmann D, Law R. On moment closures for population dynamics in continuous space. *Journal of theoretical biology*. 2004;229:421-32.
- [59] Raghil M, Hill NA, Dieckmann U. A multiscale maximum entropy moment closure for locally regulated space–time point process models of population dynamics. *Journal of Mathematical Biology*. 2011;62:605-53.
- [60] Binny RN, James A, Plank MJ. Collective cell behaviour with neighbour-dependent proliferation, death and directional bias. *Bulletin of Mathematical Biology*. 2016;78:2277-301.
- [61] Law R, Dieckmann U. A dynamical system for neighborhoods in plant communities. *Ecology*. 2000;81:2137-48.
- [62] Van Kampen NG. *Stochastic processes in physics and chemistry*. vol. 1. Elsevier; 1992.
- [63] Toral R, Colet P. *Stochastic numerical methods: an introduction for students and scientists*. John Wiley & Sons; 2014.
- [64] Murray JD. Reaction Diffusion, Chemotaxis, and Nonlocal Mechanisms. In: *Mathematical biology: I. An introduction*. vol. 17. Springer Science & Business Media; 2007. p. 395-416.
- [65] Meron E. *Nonlinear physics of ecosystems*. CRC Press, Taylor & Francis Group Boca Raton, FL, USA; 2015.